

Design, fabrication, and characterization of a liquid crystal-based large area electrically tunable lens for correction of astigmatism and defocus

Amit K. Bhowmick,^a Afsoon Jamali,^b Douglas Bryant,^a Sandro Pintz,^b and Philip J. Bos^{a,*}

^aKent State University, Material Science Graduate Program, Kent, Ohio, United States

^bMeta Platforms Inc., Reality Labs, Redmond, Washington, United States

ABSTRACT. An optical imaging system's image quality can deteriorate due to uncorrected astigmatism and defocus. An approach to correct these issues is proposed, which involves a non-mechanical, electronically adjustable system. This system consists of three liquid crystal-based cylindrical lenses, which adjust optical power depending on applied voltage values. The advantages of this system include a simple and low-cost structure, large aperture size, low-voltage drive, and compact design. This non-mechanical solution has great potential for various applications, such as wavefront correction for large telescopes, microscopy, augmented reality/virtual reality, and prescription eyeglasses. Design, fabrication, and optical characterization of the proposed device are discussed.

© The Authors. Published by SPIE under a Creative Commons Attribution 4.0 International License. Distribution or reproduction of this work in whole or in part requires full attribution of the original publication, including its DOI. [DOI: [10.1117/1.OE.62.7.075103](https://doi.org/10.1117/1.OE.62.7.075103)]

Keywords: optics; adaptive lens; defocus; tunable lens; astigmatism; liquid crystal

Paper 20230338G received Apr. 10, 2023; revised Jun. 23, 2023; accepted Jun. 28, 2023; published Jul. 12, 2023.

1 Introduction

Astigmatism and defocus are two of the major optical aberrations that can affect the performance of an optical imaging system.¹ Astigmatism arises from asymmetry in the shape of the optical system or misalignments of its components.² This results in distorted or blurred images, requiring correction for sharp focusing. On the other hand, defocus occurs when an image is not in focus, due to a mismatch between the image distance and the detector distance. Conventional correction methods for astigmatism and defocus typically involve the use of mechanically driven, bulky lenses.^{3–5} However, modern optics research aims to replace these traditional mechanical correction methods with compact, low-cost, non-mechanical solutions.⁶

In the field of adaptive optics, several methods have been developed over the past four decades to adjust the focal length of optical systems.⁷ However, only a limited number of these methods can do dynamic non-mechanical correction of astigmatism and few of them have been able to achieve large aperture size.^{8–11} One notable design, proposed by Campbell,¹² uses electrically tunable fluidic lenses to achieve dynamic correction of astigmatism, but fluidic lenses are subject to well-known problem of gravitational sagging and surface tension. Another commonly studied method is the use of liquid crystal (LC) spatial light modulators,^{13–15} but these devices are typically reflective and suffer from reduced image quality due to pixelization.¹³ In this study, we present an approach of designing a transmissive LC-based electronic lens with a large aperture (50 mm in diameter) that can electrically tune both focal length and astigmatism without the need

*Address all correspondence to Philip J. Bos, pbos@kent.edu

for mechanically moving parts. To the best of our knowledge, this is the first practical astigmatism correction device that is easy to fabricate, low-cost, flat, fast-switching (<1 s), and low-voltage driven (<5 V).

The proposed device has a compact form factor, which opens up a wide range of possibilities for its use, from large space telescopes to small-scale imaging systems. For instance, in a typical large space telescope, light is reflected from the primary mirror to the secondary mirror, which results in a sharp image if both mirrors are perfect. However, this is not always the case as imperfections such as gravity, thermal expansion, and manufacturing errors can cause astigmatism and defocus.¹⁶ A non-mechanical solution is desired to correct such astigmatism, which is where the proposed device comes in as a low-cost option. It can also be used in human eye correction glasses, microscopes, wavefront correction, cameras, and precision optics. This paper provides detailed information on the design, modeling, fabrication, and characterization of the device that is recently introduced as a theoretical concept.¹⁷

2 Device Concept

The proposed device is a stack of three tunable LC-based tunable cylindrical lenses. Each cylindrical lens utilizes a stripe pattern of electrodes on the bottom plate and continuous ground electrode on the top plate. LC material is sandwiched between bottom and top electrode plate and separated by distance d . The LC is a birefringent material whose refractive index for light polarized along the average long molecular axis (the director) is known as extraordinary refractive index (n_e), and refractive index along average short molecular axis (perpendicular to the director) is known as ordinary refractive index (n_o). The difference between these two indices is known as birefringence of the material (Δn). Due to dielectric anisotropy ($\Delta\epsilon$), the LC director orientation is sensitive to an electric field. Positive dielectric anisotropic material ($\Delta\epsilon > 0$) is used in the device, which tends to align LC director along the direction of applied electric field.

The inner conductive layer of two substrates is coated with polymer alignment layer, which sets the alignment direction of the LC director along the rubbing direction in the plane of the cell when no voltage is applied. In the presence of an electric field normal to the plane of the cell, the effective refractive index (n_{eff}) of LC material become a function of LC director orientation angle (θ), which is defined as the angle between LC director optic axis and the light propagation direction. The value of n_{eff} can be written as

$$n_{\text{eff}} = \frac{n_o n_e}{\sqrt{n_e^2 \cos^2(\theta) + n_o^2 \sin^2(\theta)}}. \quad (1)$$

The effective refractive index of the LC cell changes between n_o and n_e based on applied voltage magnitude. The change of the optical path length (OPL), when θ varies from 0 deg to 90 deg, is the maximum optical path difference (OPD) for light traveling through the LC cell of thickness d . It can be written as

$$\text{OPD}_{\text{LC}} = (n_e - n_o)d. \quad (2)$$

To achieve a high-quality cylindrical LC lens, its OPL as a function of its perpendicular distance from the symmetry axis of the lens (r) should follow parabolic phase profile. Specifically, the OPL of an ideal cylindrical lens of maximum radius R and focal length f can be written as

$$\text{OPL}(r)_{\text{ideal negative lens}} = \frac{r^2}{2f}, \quad (3a)$$

$$\text{OPL}(r)_{\text{ideal positive lens}} = \frac{(R^2 - r^2)}{2f}. \quad (3b)$$

As a result, the maximum OPD between the center and the edge of the lens become:

$$\text{OPD}(R)_{\text{ideal lens}} = \frac{R^2}{2f}. \quad (3c)$$

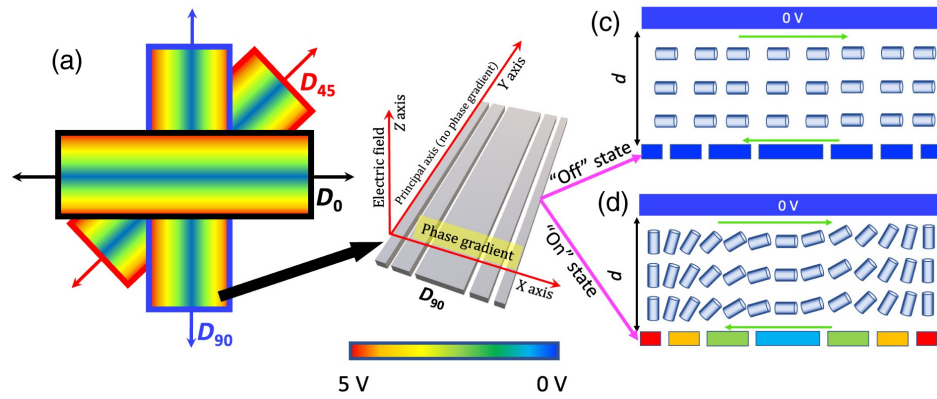


Fig. 1 (a) Schematic diagram of the dynamic astigmatism and defocus corrector device in top view. The three rectangles represent three tunable LC-based cylindrical lenses. The color change on the rectangle represents the voltage gradient in the plane of each lens. The phase gradient and principal axis of L_{90} and L_{45} are rotated by 90 deg and 45 deg, respectively, compared to phase gradient and principal axis of L_0 . (b) 3D perspective view of patterned electrode of L_{90} and (c) side view of L_{90} under no voltage application. Blue cylinders in between patterned strip electrode and common ground represent LC director orientation. Green arrow represents the rubbing direction of two plates. (d) Side view of LC director in L_{90} under voltage distribution over stripe electrodes.

The parabolic change of OPD, as shown in Eq. (3), can be achieved in the LC cell when the stripe electrodes are utilized, where the width of the electrodes changes in parabolic fashion. With the appropriate voltage distribution applied to the stripe electrodes, the parabolic variation of the OPL can be achieved. Using a concentric electrode design, near-diffraction limited optical performance has been reported by Li et al.¹⁸ for a 2.4 mm aperture size LC lens.

In the design of our device, the three cylindrical lenses are stacked in a specific manner as shown in Fig. 1(a). The second and third lenses of the device have a symmetry axis that is rotated by 90 deg and 45 deg, respectively, with respect to that of the first lens. Due to stripe shape electrode pattern, there is no change of refractive index along the symmetry axis of the patterned electrodes, but varies along an axis perpendicular to it. The symmetry axis of the cylindrical lens is shown in Fig. 1(b). The first cylindrical lens L_0 is defined as having a power of D_0 with its symmetry axis at 0 deg. The second and third cylindrical lenses, L_{90} and L_{45} are defined as having powers D_{90} and D_{45} , respectively, with their symmetry axis rotated by 90 deg and 45 deg counterclockwise. A schematic diagram of the LC director orientation for a lens “off” state and an “on” state is shown in Figs. 1(c) and 1(d), respectively, for the L_{90} lens in $X - Z$ plane. As a result of gradient refractive index along one direction, light propagating through individual cylindrical lenses of the device gives a line focus. However, with the stack of three tunable lenses in described fashion, the ability of controlling the amount of cylindrical power with a defined axis of rotation and spherical power can be achieved. In other words, the stack of three tunable cylindrical lenses acts as a tunable spherocylindrical lens, which can be realized for dynamic correction of astigmatism and defocus.

The final result of the three cylindrical lenses is to provide a spherical power (D_s), a cylindrical power (D_c), and axis (α). The equations that define D_s , D_c , and α in terms of D_0 , D_{90} , and D_{45} , derived in a separate publication,¹⁷ are

$$D_s = \frac{D_0 + D_{45} + D_{90} - D_c}{2}, \quad (4)$$

$$D_c = \sqrt{(D_0 - D_{90})^2 + D_{45}^2}, \quad (5)$$

$$\alpha = \frac{1}{2} \tan^{-1} \left(\frac{D_{45}}{D_0 - D_{90}} \right). \quad (6)$$

By changing the optical powers of the lenses L_0 , L_{45} , and L_{90} , the resulting D_s , D_c , and α can be tuned without the need of any sort of mechanical moving parts.

3 Device Design

The design of large aperture LC lenses require consideration of several factors, including shape of the phase profile, number of electrodes, gap between electrodes, switching speed, viewing angle performance, and polarization dependency, which are discussed in this section.

As discussed in the device concept, the most important factor in designing a large aperture LC lens with high quality is to achieve a parabolic change in the phase profile using stripe pattern electrodes. The stripe electrodes in the lens have a non-constant width relative to their distance from the center of the lens. The width of the electrodes varies in a parabolic fashion along the desired phase gradient axis to maintain a constant change in refractive index between electrodes and to achieve a parabolic phase profile throughout the lens aperture. There needs to be electrode gaps to achieve voltage divider circuit between the adjacent pattern electrodes. As a result, the discretization of the phase profile in LC lenses is unavoidable. More electrodes and a minimum electrode gap is favorable for reducing phase discretization. For a fixed sampling rate f_s (number of electrodes per wave), the total number of discrete electrodes (N_e) can be calculated from the following formula:

$$N_e = \text{OPD}_{\text{ideal lens}} \times \frac{2f_s}{\lambda}. \quad (7)$$

The response time of large aperture LC lenses is a crucial factor to consider in the design. Comparing Eqs. (2) and (3), it can be seen that the cell thickness of the LC lens is proportional to the square of the lens radius. Also the switching speed of LC cell is proportional to the square of its cell thickness,¹⁹ and therefore, for a given birefringence of the LC material and given optical power of the lens, the response time of LC lens is proportional to the fourth power of lens radius. However, the limitation of switching time for large aperture LC lenses can be addressed by utilizing a segmented phase profile design.²⁰⁻²⁵ This method involves dividing the phase profile of the lens into multiple parabolic phase segments, which allows an increase the lens radius without increasing the LC lens cell thickness. In this approach, maximum diffraction efficiency can be achieved when the phase difference between the segments is an integer multiple of 2π radians.²⁶ The impact of such design for a tunable LC lens is discussed in the previous work.²⁵ By restricting the cell thickness (d) of LC lens, the total number of segmented phase profile for given lens aperture size (R) and focal length (f) can be written as

$$N_s = \frac{\text{OPD}_{\text{ideal lens}}}{\text{OPD}_{\text{LC}}}. \quad (8)$$

The next design consideration of the lens system involves the effect of off-axis light propagation through the device. It is well established that the phase retardation of an LC device is dependent on the angle in which light passes through it. However, Li et al.²⁷ demonstrated that the viewing angle problem can be significantly reduced by pairing of each lens with a counterpart that is anti-parallelly rubbed. This implies that the aligned LC director of the counter lens has a tilt sense that is opposite to that of the original lens. To improve viewing angle performance with this method, each cylindrical lens in the device is a stack of two anti-parallel rubbed LC cells. In summary, the device consists of three tunable cylindrical lenses, each consisting of two cells, resulting in a total of six LC cells stacked in the device.

The example device considered in this paper is polarization dependent. However polarization independence can be achieved by duplicating each of the above considered six cells, with each duplicated cell aligned with its symmetry axis orthogonal to the original.²⁵

4 Modeling Method

The LC director field of target device is accurately modeled using the relaxation method previously described.^{17,28,29} The resulting phase profile of the device is calculated following the method also described previously.^{28,29} Finally, the far-field spot profile in the focal plane of the lens is simulated using the phase profile information and the Rayleigh Sommerfield scalar diffraction analysis method, as described by Voelz.³⁰

5 Modeling of an Example Device

In our study, we present an example device, which has clear aperture size of 5 cm. Each cylindrical lens is capable of continuously tuning its optical power from -0.80 to 0.80 D, resulting the tunable optical power range of each cylindrical lenses of 1.60 D. To maintain acceptable off axis light propagation performance, each ± 0.80 D lens consists of two separate LC cells, each with a tunable capability of ± 0.40 D. For ± 0.40 D, the maximum OPD of each cell is equal to $125 \mu\text{m}$ as calculated from Eq. (3c). To improve the switching speed of the device, 28 continuous phase segments are considered in the design where width of the segments change in parabolic fashion within entire aperture as previously reported.^{20,22,25} With 28 phase segments, maximum OPD per segment is equal to $4.46 \mu\text{m}$. The phase profile of the three cylindrical lenses of the device with 28 phase segments are shown in Figs. 2(a)–2(c). Using the LC material (MLC-2172 from Merck) with birefringence value $\Delta n = 0.2939$ and considering to use 80% of the material value as the maximum useable change in Δn , the thickness requirement of the LC cell becomes $20 \mu\text{m}$. The switching time of the lens with similar segmented phase design was as <1 s.²⁰ The desired parabolic phase profile in each segment is achieved using stripe pattern electrodes. A study by Li et al.³¹ showed that when the phase step per electrode is $<1/8$ waves, a diffraction efficiency $>95\%$ can be obtained. In the example lens considered here, the phase step per electrode is set to $1/10$ wave in the inner lens region, $1/8$ wave in the mid lens region, and $1/7$ wave in the outer lens region. This results in a total of 2730 electrodes within the entire aperture, with the center electrode width being $\sim 230 \mu\text{m}$ and the narrowest electrode width being approximately $6 \mu\text{m}$. If each lens is biased by adding a fixed power lens of $+0.80$ D, then the continuous tunability range will be shifted, resulting tunable optical power between 0 and 1.60 D. In the device discussed in this paper, a bias lens with a power of $+0.75$ D is used. This results in the minimum and maximum optical power of each lens being -0.05 and $+1.55$ D, respectively.

As it is the astigmatism correction that represents the novel feature of the device design considered here, in this section, the maximum astigmatism correction for the example lens is shown with the spherical power of the device (D_s) set to 0 D, and the ability to change the axis of the cylindrical power is demonstrated. With the designed example LC lenses, maximum cylindrical power that allows any value of α is 1.35 D. In Fig. 3, the simulated results for seven values of α are shown. The optical power configuration of the three cylindrical lenses for the corresponding cases are listed in Table 1. It is important to note that the simulation results only show the results at the center of the lens within 5 mm wide aperture, which do not include the effects of the segmented phase profile. As a result, any discrete power state of the cylindrical lenses will give close to diffraction-limited optical performance. However, in the periphery of the lens, the optical performance will be slightly degraded due to LC director distortion at the phase reset boundaries, which causes haze. If steps are taken, such a haze effect of the phase segmentation can be reduced.³²

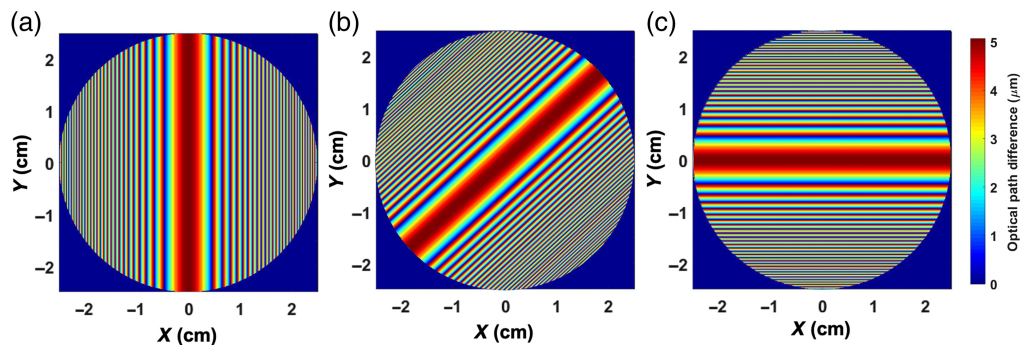


Fig. 2 Phase maps of designed individual 5 cm diameter cylindrical lenses with 28 phase segments. From the same viewpoint of Fig. 1(a), (a)–(c) represent cylindrical lenses that have symmetry axis along 0 deg, 45 deg, and 90 deg, respectively.

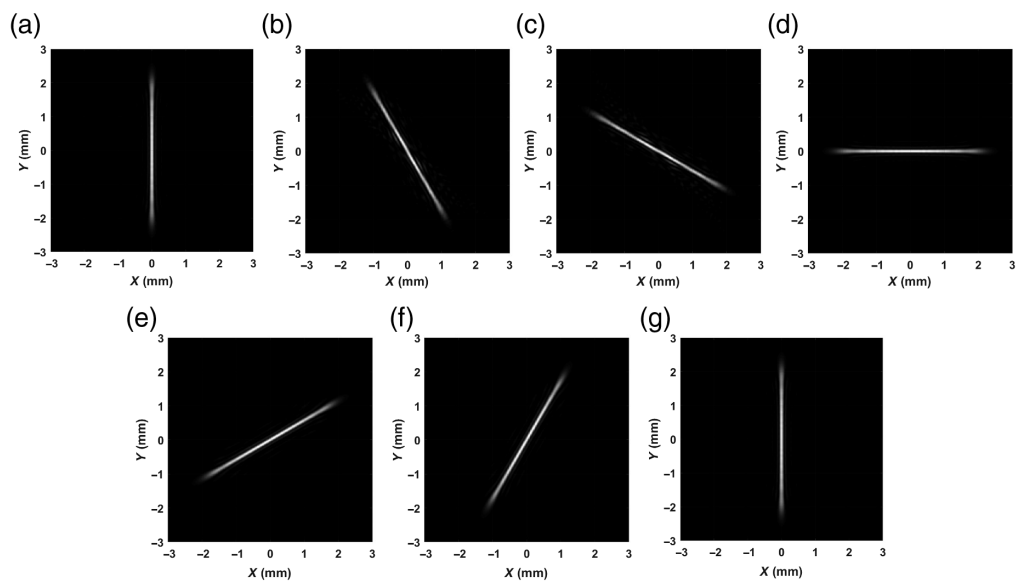


Fig. 3 1.35 D dynamic astigmatism correction in every 30 deg of principal axis. (a)–(g) 1.35 D astigmatic power with principal axis angle α equal to -90 deg, -60 deg, -30 deg, 0 deg, 30 deg, 60 deg, and 90 deg, respectively. Optical power configuration in L_0 , L_{45} , and L_{90} for each case is shown in Table 1.

Table 1 List of optical powers on the three cylindrical lenses of the device for resulting $D_c = 1.35$ D astigmatic power in every 30 deg principal axis variation.

Optical power in lenses	Angle of principle axis for 1.35 D astigmatic power						
	-90 deg	-60 deg	-30 deg	0 deg	30 deg	60 deg	90 deg
L_0 (D)	0	0.92	1.60	1.35	0.42	-0.25	0
L_{45}	0	-1.16	-1.16	0	1.16	1.16	0
L_{90}	1.35	1.60	0.92	0	-0.25	0.42	1.35

6 Device Fabrication

6.1 Driving Scheme

The driving mechanism of the designed LC lens involves utilization of an inter-electrode resistor network between all the electrodes in a continuous phase segment, similar to previous concentric ring electrode-based lens design.^{22,24,25,31} As the electrode shape changes in parabolic fashion, a constant phase drop in the electrodes is required to maintain parabolic phase profile. The resistors create a voltage divider circuit, which gives a fixed voltage step between adjacent electrodes. If phase change versus applied voltage relationship is linear in the LC material, then only two end electrodes of the resistor network will be enough to control the parabolic phase profile of a continuous phase segment. However, the voltage-to-phase change in LC material is non-linear, making it difficult to control the phase profile with only two input voltages. To overcome this, eight input voltages are utilized in the device, making the phase-voltage relationship approximately linear within the eight voltages. Hence, only eight input voltages are applied to each phase segment that has more than 50 electrodes. A schematic diagram of the stripe electrodes with resistors is shown in Fig. 4. To achieve the continuous phase change within the entire aperture, the same eight voltages are applied to each continuous phase segment of the lens. The input voltages are carried by buslines, which connect the addressable stripe electrode through via interconnect.

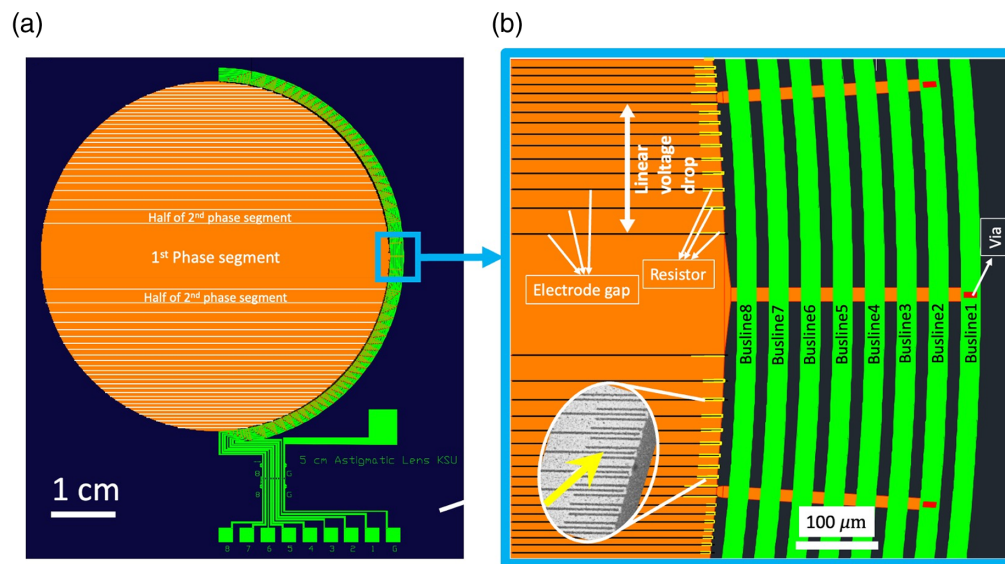


Fig. 4 (a) Photomask layout of the cylindrical lenses. The orange color represents the stripe electrodes within the active area and the green color shows the buslines that supply voltages to the phase segments. The white line on the active area presents the position of the boundaries of the continuous phase segments. (b) Zoomed view of the blue square region of (a), the red square represents the position of via interconnect on the photomask. The resistors on the stripe electrodes are represented by yellow color schematically. On the bottom left corner of this figure, resistors in a fabricated cell are indicated by yellow arrow within the zoomed area.

Top view of the mask diagram of the designed cylindrical LC within entire lens area is shown in Fig. 4(a) and closer look at the center lens area is shown in Fig. 4(b). Yellow, orange, red, and green color regions represent the resistors, stripe electrodes, via interconnect, and busline connection, respectively. Positions of the boundaries of the segmented phases over the entire aperture region are indicated by white solid lines in Fig. 4(a).

6.2 Fabrication Steps

The process of fabricating cylindrical lenses for the device involves several steps, including photolithography, sputtering deposition, and standard LC cell assembly techniques. The patterned stripe electrodes in the lens are transparent indium tin oxide (ITO) layers, and nickel is used as the busline due to its high conductivity. The buslines are positioned outside of the active area as nickel blocks light transmission. The connection between the ITO electrodes and the applied voltage is achieved through a via interconnect in the patterned silicon dioxide (SiO_2) insulator layer.

The fabrication process begins with patterning the bottom ITO-coated glass substrate for the stripe electrodes using a stripe electrode photomask. Then SiO_2 layer of thickness 300 nm deposited on top of the ITO electrodes using a vacuum sputtering machine. The SiO_2 layer is then patterned using a via interconnect photomask and etched at the via location within small rectangle area ($10 \mu\text{m} \times 10 \mu\text{m}$) using a reactive ion dry etching process. Then nickel layer of sheet resistance ~ 1 ohms/sq. is deposited on top of the SiO_2 layer using a vacuum sputtering machine and patterned to create busline connections (width $10 \mu\text{m}$). A polyimide (SE-2170) layer is spun-coated on top of the patterned plate, and after soft baking at 80°C for 5 min and hard baking at 200°C for 1 h, the plate is rubbed to create a pretilt angle of ~ 3 deg. The remaining fabrication steps are standard in the display industry, which include spraying spacers, assembling the top and bottom plates using thermal cured glue, vacuum filling with LC material, and end sealing. Finally, the Ni buslines are connected to a flex cable using anisotropic conductive tape for ease of driving the cells. This step-by-step fabrication process is shown in side view of different layers in Fig. 5(a) and in top view in Fig. 5(b).

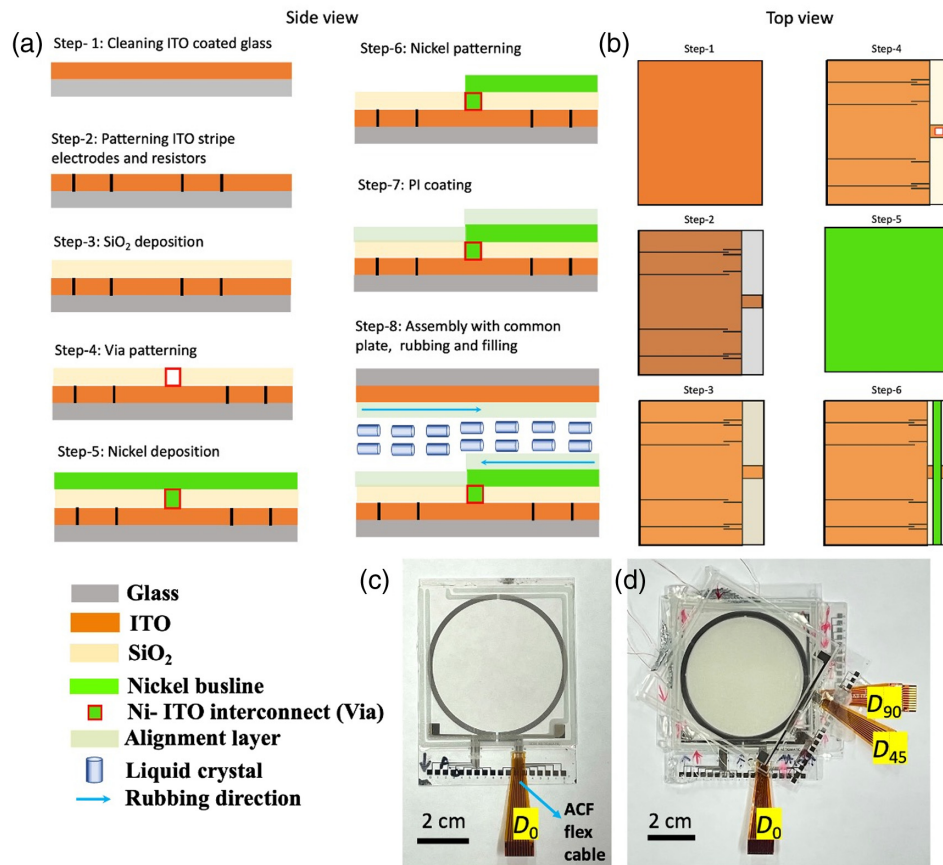


Fig. 5 (a), (b) Schematic diagram of step-by-step fabrication process of a lens cell of the proposed device in side view and top view, respectively. On the lower right, definition of the different layers of cell schematic diagram is provided. (c) Top view of the one fabricated LC cell and (d) top view of the device (stack of three cylindrical LC lenses).

7 Device Characterization

7.1 Phase Profile Characterization

In order to adjust the voltage profile of the lenses, the phase response of the built LC cell is measured for different applied voltages. The relationship between phase and voltage depends on the thickness of the LC lens. For a designed LC lens thickness ($20 \mu\text{m}$), first phase versus voltage curve is measured. The best region with a linear relationship between phase and voltage is chosen from the measured curve and is divided into eight equally spaced intervals. The eight voltages are applied to the eight buslines that can be varied to control the optical power of each lens. Here the phase profile of the device is measured with the voltage profile to provide $+0.80 \text{ D}$. The phase profile [Fig. 6(a)] is obtained by passing white light through a color filter ($\lambda = 543.5 \text{ nm}$) and the LC lens device placed at 45° between cross polarizers. The phase modulation of the fabricated cell is compared to an ideal lens phase modulation curve of equal optical power and shown in Fig. 6(b). The changes in phase profile for five different LC lens operating cases are shown in Figs. 6(c)–6(g).

7.2 Device Demonstration and Modulation Transfer Function Measurement

To evaluate the device's potential for white light application, we utilized a 1951 USAF chrome eyechart back-illuminated by a uniform white light. The light passed through the air force chart and a polarizer oriented parallel to the device's rub direction. Images formed without the presence of the device and with device (in operating state) were captured using a Canon 450D DSLR with a 100 mm macrolens. The aperture stop of the DSLR lens was maintained at $f2.8$, and a 5 mm physical aperture stop was attached to the lens aperture. To maintain consistency with

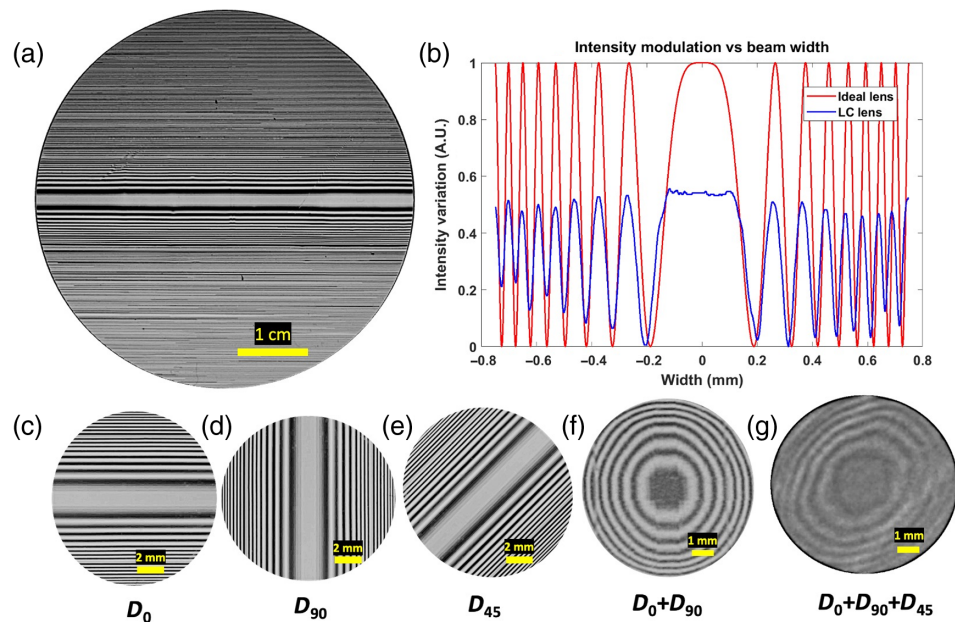


Fig. 6 (a) Phase profile of single cell within entire aperture when voltage profile is tuned for $+0.40$ D. In the optical setup, the fabricated cell is placed between cross polarizers and the rubbing direction of the cells are along 45 deg to cross polarizers. (b) Intensity modulation plot of the built lens cell compared to an ideal curve of the same optical power within first segmented phase region. Red and blue solid curves represent intensity modulation for ideal lens case and LC lens case, respectively. Positions of the interference fringes is the main consideration of this comparison. (c)–(g) The phase modulation when power configurations of the three lenses on the device are ($L_0 = 0.40$ D, $L_{45} = 0$ D, $L_{90} = 0$ D); ($L_0 = 0$ D, $L_{45} = 0$ D, $L_{90} = 0.40$ D); ($L_0 = 0$ D, $L_{45} = 0.40$ D, $L_{90} = 0$ D); ($L_0 = 0.40$ D, $L_{45} = 0$ D, $L_{90} = 0.40$ D); and ($L_0 = 0.40$ D, $L_{45} = 0.40$ D, $L_{90} = 0.40$ D), respectively.

our modeling, we have targeted that the three cylindrical lens powers (D_0 , D_{45} , and D_{90}) in the device have the same power range as modeled. The power range of 1.55 D is obtained by tuning three lenses to an optical power of $+0.80$ D and attaching three high-quality cylindrical glass lenses with a fixed optical power of $+0.75$ D to each lens with their symmetry axis parallel to each lens (Fig. 7).

Three cases are considered to assess the device's ability to correct optical aberration in a white light image. In the first case, we captured an image of the USAF eyechart with only white light passing through the polarizer and the USAF chrome target, as shown in Fig. 8(a). In the second case, we intentionally introduced optical aberration into the USAF eyechart image using two sets of high-quality lenses: a -1.50 D spherical lens and a -1.50 D cylindrical lens with

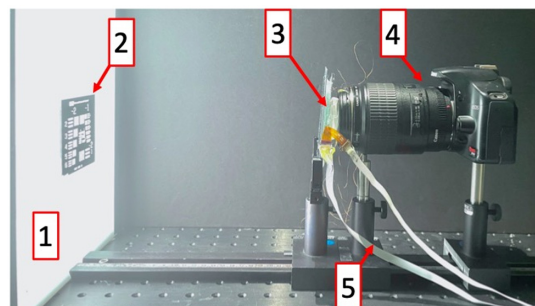


Fig. 7 Experimental optical setup for imaging resolution test. (1) Fluorescence light source, (2) chrome on glass USAF 1951 test target, (3) LC lens device with polarizer (polarization axis parallel to LC device rubbing direction), (4) Canon 450D DSLR camera with 100 mm macro lens, and (5) Ribbon cables going to voltage driver.

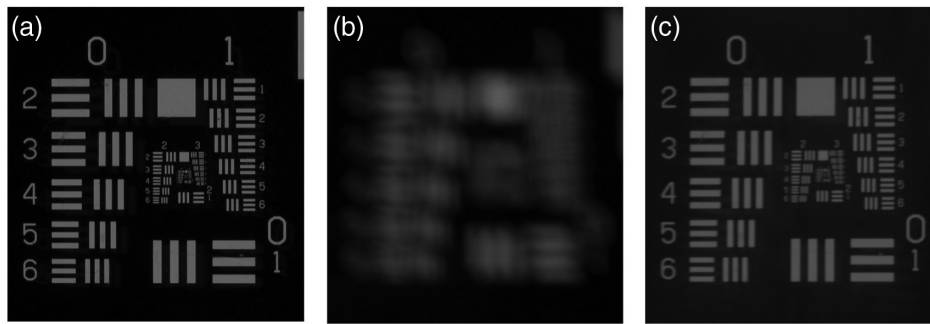


Fig. 8 Evaluation of the device for white light application: image of the air force chart (a) taken without the presence of the device, (b) when optical aberration is imposed by -1.50 D spherical lens and -1.50 D cylindrical lens with principal axis along 45 deg, and (c) after correcting optical aberration using the built device. Optical power of the three cylindrical lenses of the device in this case are $+1.55$ D each, which led to resultant spherical power to be $+1.55$ D, resultant cylindrical power to be $+1.55$ D, and resultant principal axis to be 45 deg.

the principal axis along 45 deg. This resulted in an aberrated USAF eyechart image [Fig. 8(b)] when captured with the DSLR camera without altering any settings from case 1. In the third case, we applied voltage to the LC lenses in our device to ensure that all three lenses had an optical power of $+1.55$ D. This configuration resulted in a spherical power of $+1.55$ D and a cylindrical power of $+1.55$ D with a principal axis angle of 45 , as calculated from Eqs. (4)–(6), respectively. The image is captured using the DSLR camera without modifying any settings from the previous case, as shown in Fig. 8(c). Our observations indicate that our device corrected the imposed optical aberration, resulting in a focused and astigmatism-free image.

Image resolution of the built device is evaluated within 5 mm diameter at center of the device. In order to quantify image quality, we measured modulation transfer function (MTF) by measuring contrast ratio around group (1) element (1) of eyechart, which corresponds to spatial resolution 10 cyc/deg based on the distance from the lens and the USAF target. The contrast ratio is calculated by taking intensity variation of maximum intensity (I_{\max}) and minimum intensity (I_{\min}), divided by the sum of I_{\max} and I_{\min} . We compared the MTF for the case when the device is not present and for the case when the device is added to correct the imposed optical aberration. Specifically, we have compared MTF at spatial frequency 10 cyc/deg for Figs. 8(a) and 8(c). Intensity variation plot of group (1) element (1) from Figs. 8(a) and 8(c) is shown in Figs. 9(a) and 9(b), respectively. The measured MTF value decreased to 0.62 when the device was used to correct the aberration, compared to the MTF value of 0.90 when the device was not present. Comparison of measured MTF with respect to diffraction limited MTF is shown in Fig. 9(c) at two optical power states $+0.40$ and $+0.80$ D. Such large drop of MTF when LC lenses are at maximum power state ($+0.80$ D) can be explained by overall haze induced by the device from multiple sources, such as electrode gap and silica spacers, reflection from the surfaces of the individual cells of the device stacks. The main source of the haze and degradation of the MTF in this case is caused by the gaps between the striped electrodes. Previous reports have demonstrated that this problem can be basically eliminated by implementing floating electrodes¹⁸ that are an addition electrode layer placed on top of the electrode gap region. With floating electrodes, a lower spacer density, and optical coupling of the stacked cells, the overall haze of the device would be significantly reduced.

Although this demonstration only shows astigmatism correction along 45 deg, the earlier report¹⁷ shows the agreement of the physical device performance with the modeled one where other angles were evaluated (Fig. 10).

7.3 Demonstration of Dynamic Focusing and Point Spread Function Measurement

To demonstrate the focusing effect of the device on spot profiles, an experimental setup is used to measure point spread function (PSF). This setup involves passing a He–Ne laser beam of 543.5 nm wavelength through a polarizer, a neutral density filter, a $10\times$ beam expander, a 5 mm size physical aperture stop, and the device. The polarization axis of the polarizer is aligned

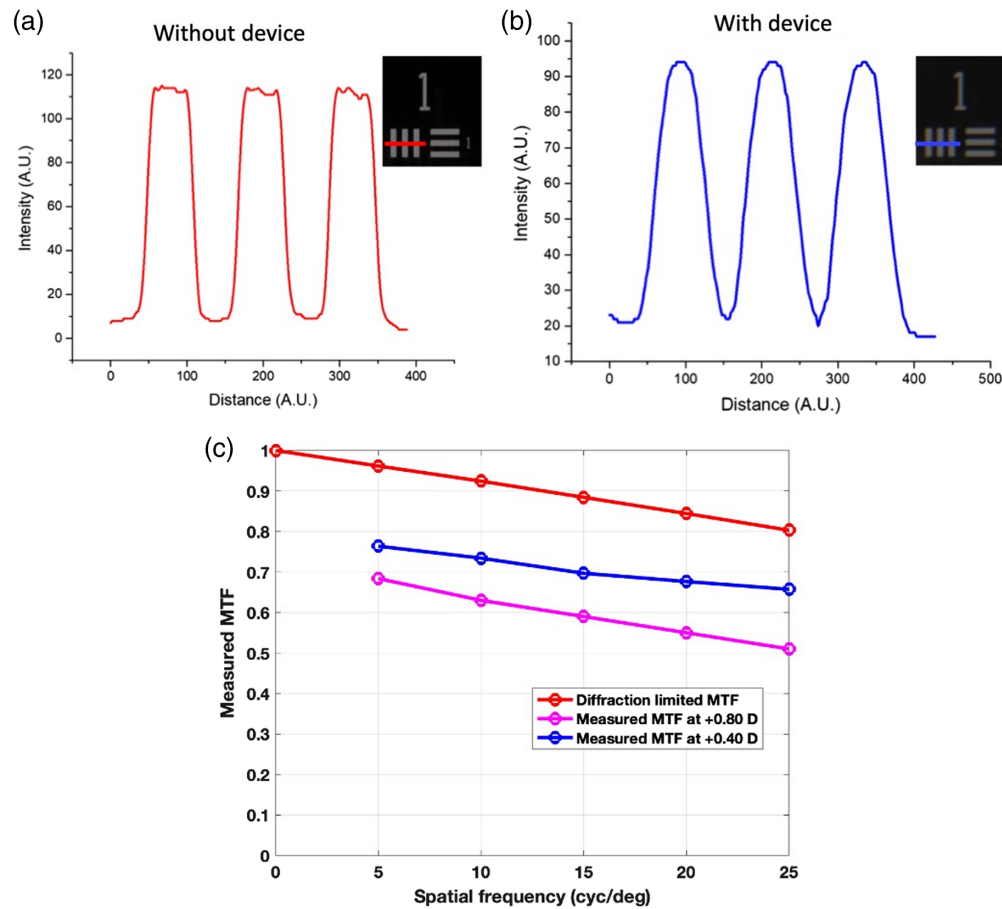


Fig. 9 Direct MTF measurement under white light condition. According to the optical setup group (1), element (1) corresponds to 10 cyc/deg. (a) Intensity modulation plot along red line of group (1) element (1) for without device case as shown in Fig. 8(a). (b) Intensity modulation plot along blue line of group (1) element (1) at with device utilized case as shown in Fig. 8(c). (c) Comparison of measured MTF with diffraction limited MTF at +0.40 D and +0.80 D optical power states.

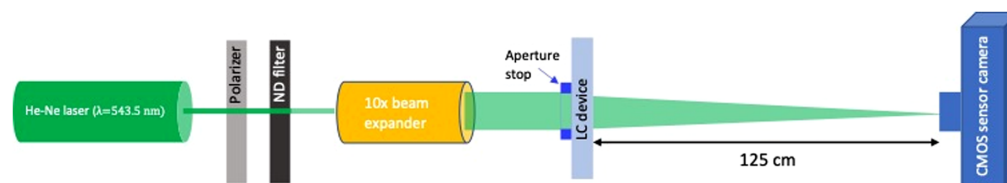


Fig. 10 Optical setup for measuring PSF of the device.

with the common rubbing axis of the lenses. The images of transmitted beam for device used case and device non-used case are captured using Canon Rebel XSI 450D, which has CMOS sensor with each pixel size of $5.2 \mu\text{m}$. The schematic diagram of the optical setup of PSF measurement is shown in Fig. 9. Figure 11(a) shows the image of the 5 mm wide beam captured without the device at the CMOS detector located at a distance of 125 cm. In Fig. 11(b), the image is captured at the same distance but with the crossed cylindrical LC lenses (L_0 and L_{90}) of the device tuned at +0.80D, whereas the L_{45} lens remains at 0 D state. At this optical power configuration, the resultant optical power contains only the spherical component, which led to $D_s = +0.80\text{D}$ and $D_c = 0\text{D}$, resulting in the convergence of the 5 mm beam size to a smaller beam (yellow ring compared to red ring) at the detector plane. The resolution of the spot profile in Fig. 11(b) is compared with a diffraction-limited spot profile in an earlier report,¹⁷ but it is repeated in this paper to demonstrate the device’s focusing capability and optical performance.

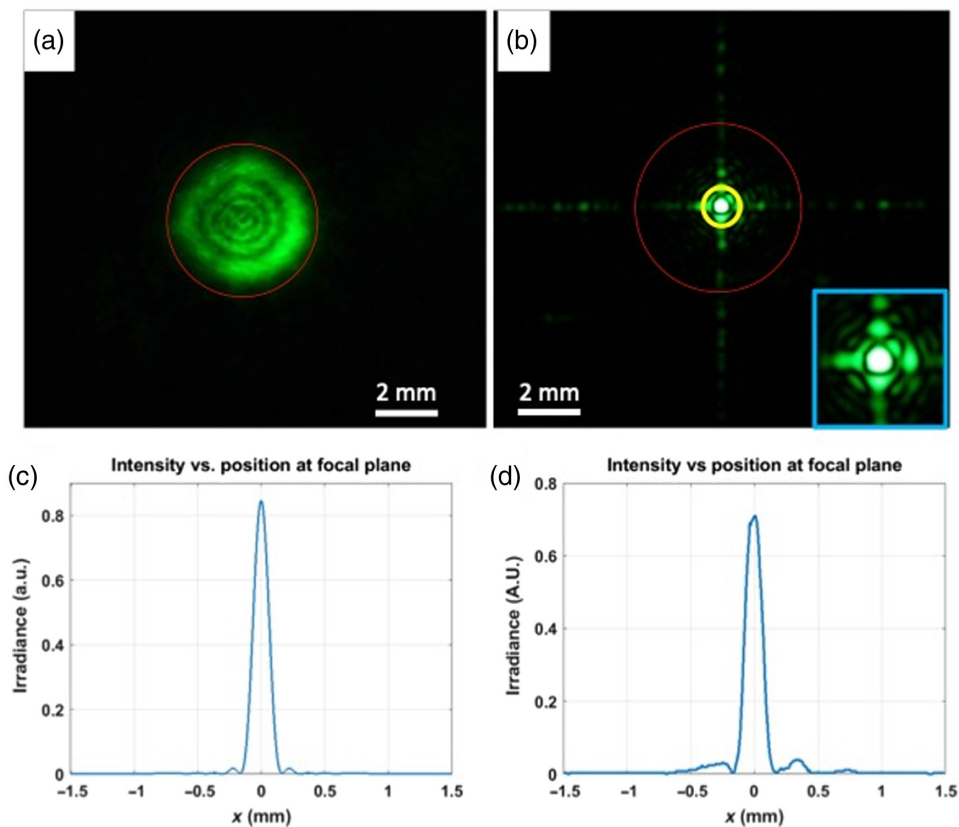


Fig. 11 Demonstration of focus correction, measured PSF, and comparison of PSF with diffraction limited PSF. (a) The 5 mm beam shape is captured on the CMOS detector at 125 cm distant from the aperture stop without the LC device. The red circle represents the original beam size. (b) When LC device is placed in front of the aperture stop and L_0 , L_{90} lenses of the device are tuned at $+0.80$ D while L_{45} is at 0 D state. The yellow circle highlights the converged beam size. Zoomed view of the spot is shown within blue square box inset: (c) numerically calculated diffraction limited PSF for the case L_0 and L_{90} are $+0.80$ D and L_{45} is 0 D and (d) measured PSF for the same power configuration using the constructed lenses.

A diffraction-limited lens with an optical power of $+0.80$ D has a first lobe diameter of $320 \mu\text{m}$ in its Airy pattern. When comparing this to the first lobe diameter from numerically calculated [Fig. 11(c)] and fabricated devices [Fig. 11(d)], the diameter of the first lobe is measured as $320 \mu\text{m}$ for the numerically calculated device and $330 \mu\text{m}$ for the fabricated device.

In Table 2, the voltage distribution on the input voltages of the LC cells at ± 0.80 D is shown. Here only the extreme values of the optical power of the lenses are shown but by changing the voltage distribution over the buslines the discussed device can be continuously tuned for dynamic correction of focus and astigmatism.

Table 2 Voltage distribution on the LC lens at different optical power states.

Optical power		Voltage distributed over buslines (BL)							
		BL1 (V)	BL2 (V)	BL3 (V)	BL4 (V)	BL5 (V)	BL6 (V)	BL7 (V)	BL8 (V)
+0.80 D	Cell 1 (+0.40 D)	0.65	1.19	1.36	1.64	1.87	2.15	2.55	3.91
	Cell 2 (+0.40 D)	0.65	1.15	1.35	1.59	1.82	2.11	2.48	3.98
-0.80 D	Cell 1 (-0.40 D)	4.85	3.18	2.52	2.17	1.88	1.64	1.46	1.08
	Cell 2 (-0.40 D)	4.85	3.15	2.45	2.07	1.81	1.66	1.42	1.11

8 Discussion

The device considered in this study composed of a stack of six LC lens cells. Each cell was constructed with stripe electrodes separated by a uniform electrode gap of $2\ \mu\text{m}$. Figure 9(c) indicates a deviation in the optical quality of the device from its theoretically predicted diffraction-limited performance. This discrepancy can be attributed to the presence of the gaps between the electrodes. Previous studies involving similar LC lens devices have shown that the use of floating electrodes can mitigate the effects of the electrode gap, thereby enhancing the MTF.

From Table 2, it is observed that the tuned voltage profiles of two distinct cells (at the same optical power) exhibit minor discrepancies. These inconsistencies can be minimized by standardizing the properties of the thin film coating, such as the coating thickness and resistivity.

The thickness of the liquid crystal layer in the cells is crucial for maintaining a consistent phase response across all cells. Nevertheless, it was found that even with a thickness variation of 10%, the fluctuation in optical power is below 0.125 D, and a lower degree of variation is easily achievable.

9 Conclusion

Most common optical aberrations in any optical device are related to astigmatism or defocus. Low-cost non-mechanical correction of both aberrations has been a long-time desire. The proposed device, presented in this paper, can be realized as a potential solution for the correction of astigmatism and defocus for large and small aperture devices. The proposed device is compact, simple, flat, low-cost, easy-to-fabricate and requires only low-voltage drive.

Acknowledgment

The project was funded by Meta Platforms Inc., Reality Labs.

References

1. E. Hecht, *Optics*, Addison-Wesley (2001).
2. W. F. Harris, "Astigmatism," *Ophthalmic Physiol. Opt.* **20**(1), 11–30 (2000).
3. G. G. Stokes and G.G. Stokes, *On a Mode of Measuring the Astigmatism of a Defective Eye*, pp. 172–175, Cambridge University Press (2010).
4. J. P. Foley and C. Campbell, "An optical device with variable astigmatic power," *Optom. Vis. Sci.* **76**(9), 664–667 (1999).
5. W. F. Harris, "The Jackson cross-cylinder. Part 1: properties," *Afr. Vis. Eye Health* **66**(2), 41–55 (2007).
6. H. Ren and S.T. Wu, *Introduction to Adaptive Lenses*, pp. 1–274, Wiley (2012).
7. L. Chen et al., "Electrically tunable lenses: a review," *Front. Robot. AI* **8**, 678046 (2021).
8. M. Ghilardi et al., "Smart lenses with electrically tuneable astigmatism," *Sci. Rep.* **9**(1), 16127 (2019).
9. D. Kopp and H. Zappe, "Tubular astigmatism-tunable fluidic lens," *Opt. Lett.* **41**(12), 2735–2735 (2016).
10. S. Y. Lee et al., "Microlens with tunable astigmatism," *IEEE Photonics Technol. Lett.* **19**(18), 1383–1385 (2007).
11. P. Liebetraut et al., "Elastomeric lenses with tunable astigmatism," *Light Sci. Appl.* **2**, e98 (2013).
12. C. E. Campbell, "Sphero cylindrical eye refraction system using fluid focus electrostatically variable lenses," U. S. Patent No. 7,826,146-B2 (2010).
13. G. D. Love, "Wave-front correction and production of Zernike modes with a liquid-crystal spatial light modulator," *Appl. Opt.* **36**(7), 1517 (1997).
14. J. D. Schmidt, M. E. Goda, and B. D. Duncan, "Aberration production using a high-resolution liquid-crystal spatial light modulator," *Appl. Opt.* **46**(13), 2423–2433 (2007).
15. X. Wang, "Performance evaluation of a liquid-crystal-on-silicon spatial light modulator," *Opt. Eng.* **43**(11), 2769–2769 (2004).
16. D. Garoli et al., "Mirrors for space telescopes: degradation issues," *Appl. Sci.* **10**(21), 7538 (2020).
17. A. K. Bhowmick et al., "Dynamic correction of astigmatism," *Appl. Opt.* **62**(7), 1791–1799 (2023).
18. L. Li et al., "Near-diffraction-limited and low-haze electro-optical tunable liquid crystal lens with floating electrodes," *Opt. Express* **21**(7), 8371–8371 (2013).
19. D. K. Yang and S.T. Wu, *Fundamentals of Liquid Crystal Devices*, pp. 1–570, Wiley (2014).
20. A. Bhowmick et al., "Wide aperture (50 mm), compact, and high-quality continuous focus tunable gradient refractive index (GRIN) liquid crystal lenses," *Proc. SPIE* **12217**, 1221708 (2022).

21. A. K. Bhowmick et al., "Large aperture 0 D-2.5D tunable liquid crystal (LC) lens based on segmented phase profile for tunable focus application," *Proc. SPIE* **12023**, 1202303 (2022).
22. A. K. Bhowmick et al., "31-5: Student paper: liquid crystal based 5 cm adaptive focus lens to solve accommodation-convergence (AC) mismatch issue of AR/VR/3D displays," in *SID Symp. Digest of Tech. Papers*, Vol. 52, pp. 410–413 (2021).
23. A. K. Bhowmick et al., "16-1: Student paper: optical performance characterization of 5 cm aperture size continuous focus tunable liquid crystal lens for resolving accommodation-convergence mismatch conflict of AR/VR/3D HMDs," in *SID Symp. Digest of Tech. Papers*, Vol. 53, pp. 166–169 (2022).
24. A. Jamali et al., "Large area liquid crystal lenses for correction of presbyopia," *Opt. Express* **28**(23), 33982–33993 (2020).
25. A. Jamali et al., "Design of a large aperture tunable refractive Fresnel liquid crystal lens," *Appl. Opt.* **57**(7), B10 (2018).
26. G. J. Swanson, "Binary optics technology: the theory and design of multi-level diffractive optical elements," *Contract*, 1-53 (1989).
27. L. Li et al., "Speed, optical power, and off-axis imaging improvement of refractive liquid crystal lenses," *Appl. Opt.* **53**(6), 1124–1131 (2014).
28. L. Li et al., "3.3: Design and modeling of a refractive liquid crystal lens for tunable optical correction in 3D stereoscopic displays," in *SID Symp. Digest of Tech. Papers*, Vol. 42, pp. 9–12 (2011).
29. L. Shi et al., "Modeling and design of a tunable refractive lens based on liquid crystals," in *Front. in Opt. 2010/Laser Sci. XXVI*, Optica Publishing Group, Rochester, New York (2010).
30. D. G. Voelz, *Computational Fourier Optics: A MATLAB Tutorial*, SPIE Press, Bellingham, WA (2011).
31. L. Li, D. Bryant, and P. J. Bos, "Liquid crystal lens with concentric electrodes and inter-electrode resistors," *Liq. Cryst. Rev.* **2**(2), 130–154 (2014).
32. A. Bhowmick et al., "Haze reduction in a large aperture liquid crystal lens with concentric electrodes and a segmented phase profile," To be submitted.

Biographies of the authors are not available.